Science Advances

AAAS

advances.sciencemag.org/cgi/content/full/4/3/eaao1761/DC1

Supplementary Materials for

High-capacity aqueous zinc batteries using sustainable quinone electrodes

Qing Zhao, Weiwei Huang, Zhiqiang Luo, Luojia Liu, Yong Lu, Yixin Li, Lin Li, Jinyan Hu, Hua Ma, Jun Chen

Published 2 March 2018, *Sci. Adv.* **4**, eaao1761 (2018)
DOI: 10.1126/sciadv.aao1761

This PDF file includes:

- fig. S1. Illustration of rechargeable aqueous ZBs using quinone electrodes.
- fig. S2. Electrochemical properties of other quinone compounds.
- fig. S3. LUMO energy and average discharge potential of different quinone compounds.
- fig. S4. CV curves of Zn-C4Q battery at 0.5 mV s^{-1} for 100 cycles.
- fig. S5. CV curves of other quinone compounds.
- fig. S6. The uptake of the fourth Zn ion in the molecular structure of C4Q.
- fig. S7. Discharge and charge curves of Zn-C4Q battery at 5 mA g^{-1}.
- fig. S8. Raman characterizations of Zn-C4Q batteries.
- fig. S9. Ex situ XRD characterizations of Zn-C4Q batteries.
- fig. S10. TEM characterization of C4Q electrode after discharge.
- fig. S11. TEM characterization of C4Q electrode after charge.
- fig. S12. Composition of Nafion.
- fig. S13. SEM images of the prepared C4Q cathode on titanium foil.
- fig. S14. Capacity retention and zinc utilization using different loading masses of C4Q.
- fig. S15. Electrochemical performance of Zn-C4Q batteries in organic electrolyte.
- fig. S16. Digital photos of the Zn anode, separator (filter paper or Nafion membrane), and C4Q cathode after cycling.
- fig. S17. Characterization of the zinc anode after cycling using a filter paper separator.
- fig. S18. SEM images of electrodes before and after cycles.
- fig. S19. Rate performance of Zn-C4Q batteries with a Nafion separator.

- fig. S20. Galvanostatic discharge and charge curves with selected cycles at 500 mA g^{-1} and corresponding energy efficiency.
- fig. S21. Cycling performance of Zn-C4Q battery using C4Q cathode with a higher conductive carbon ratio (60 wt %).
- fig. S22. Exhibition of pouch cells.
- fig. S23. Digital photo and SEM image of the zinc anode after cycling in pouch cells.
- fig. S24. Digital photos of designed batteries after in situ UV-vis spectrum collections.
- fig. S25. Selected two-dimensional UV-vis spectra.
- fig. S26. ^{1}H NMR spectra of different electrolytes after cycling in batteries used for the UV-vis test.
- fig. S27. Membrane potential tests.
- fig. S28. EIS of Zn-C4Q batteries.
- fig. S29. Electrochemical performance of aqueous Mg-C4Q batteries.
- fig. S30. Structure of C4Q after uptake of three Mg ions.
- table S1. Maximum specific capacity and lowest discharge/charge gap of electrodes coupled with metal zinc in aqueous batteries.

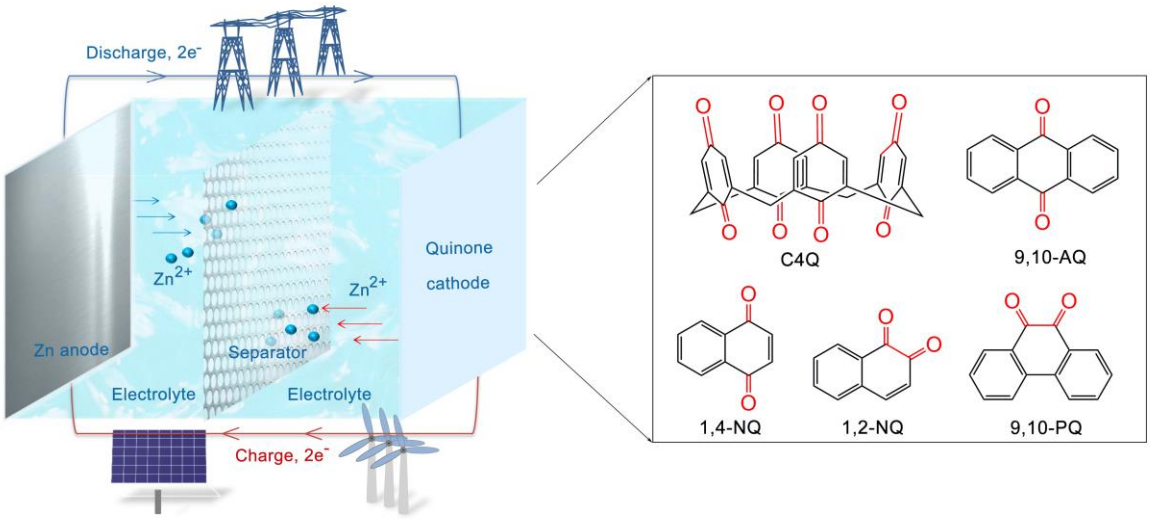

fig. S1. Illustration of rechargeable aqueous ZBs using quinone electrodes. The Zn foil is applied as anode. The porous filter paper or cation-selective Nafion membrane acts as a separator. Quinone compounds work as the cathode materials. The cartoon on the top represents the smart grids, acting as a prospect of electric power supply in discharge process. The bottom cartoons stand for the solar and wind power, acting as a prospect of electric power storage in charge process.

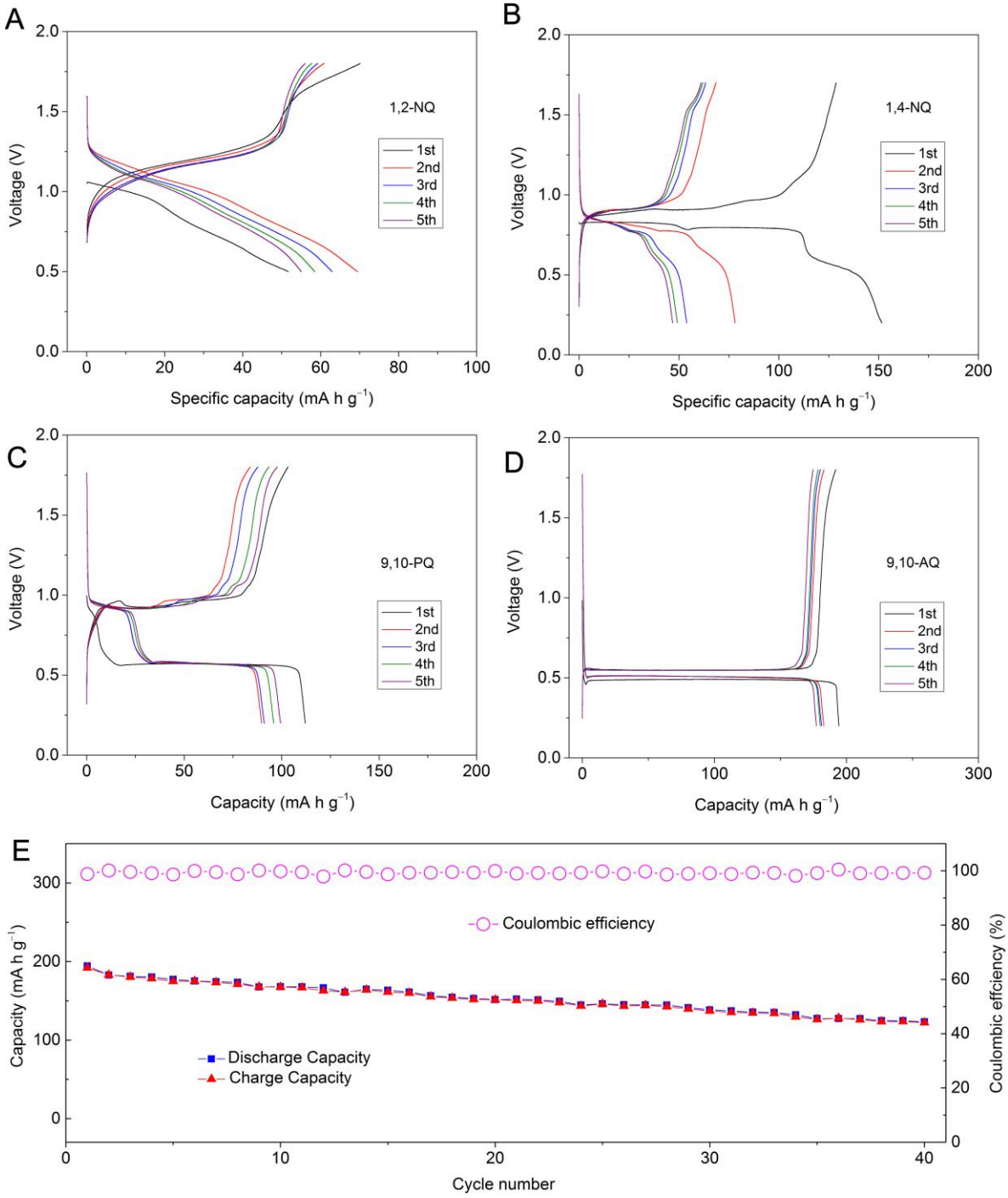

fig. S2. Electrochemical properties of other quinone compounds. The first five galvanostatic discharge and charge curves of (**A**) Zn–1,2-naphthoquinone (1,2-NQ) battery, (**B**) Zn–1,4-naphthoquinone (1,4-NQ) battery, (**C**) Zn–9,10-phenanthrenequinone (9,10-PQ) battery and (**D**) Zn–9,10-anthraquinone (9,10-AQ) battery. The current density is 20 mA g^{-1}. (**E**) Cycling performance of Zn–9,10-AQ battery at current density of 20 mA g^{-1}.

The results are obtained using filter paper as separator. The theoretical capacity of 1,2-NQ, 1,4-NQ, 9,10-PQ and 9,10-AQ calculated by the number of carbonyls are 339, 339, 258 and 258 mA h g^{-1}, separately. The utilizations of carbonyls in 1,2-NQ, 1,4-NQ, 9,10-PQ and 9,10-AQ are 20%, 44%, 43%, 75%. The reactions mechanism of 1,2-NQ should be single phase reaction, which results in no plateaus, while the reactions mechanism of 1,4-NQ, 9,10-AQ, 9,10-PQ and C4Q should two phases reaction, which leads to flat plateaus (*50*). The capacity drops of these quinones are caused by the dissolution of discharge products (organic zinc salts) in the electrolyte.

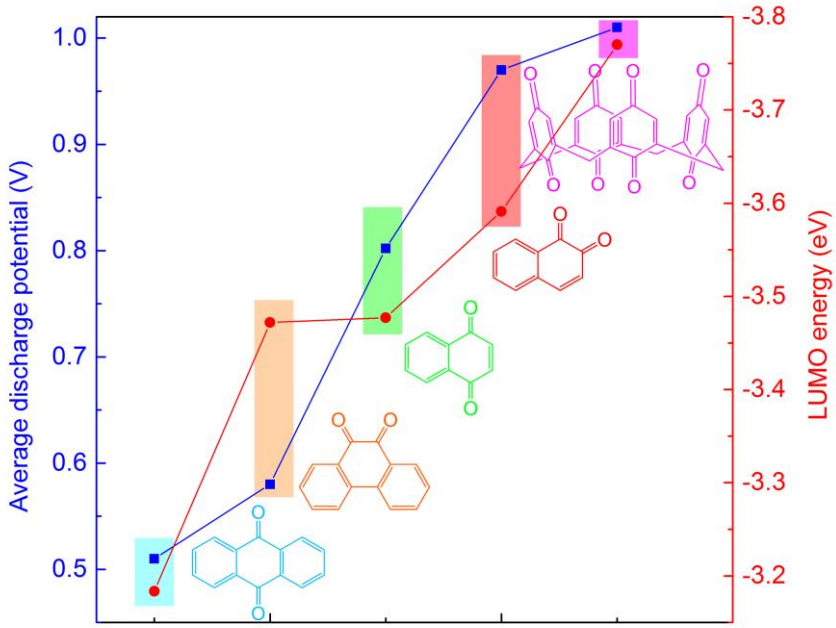

fig. S3. LUMO energy and average discharge potential of different quinone compounds.

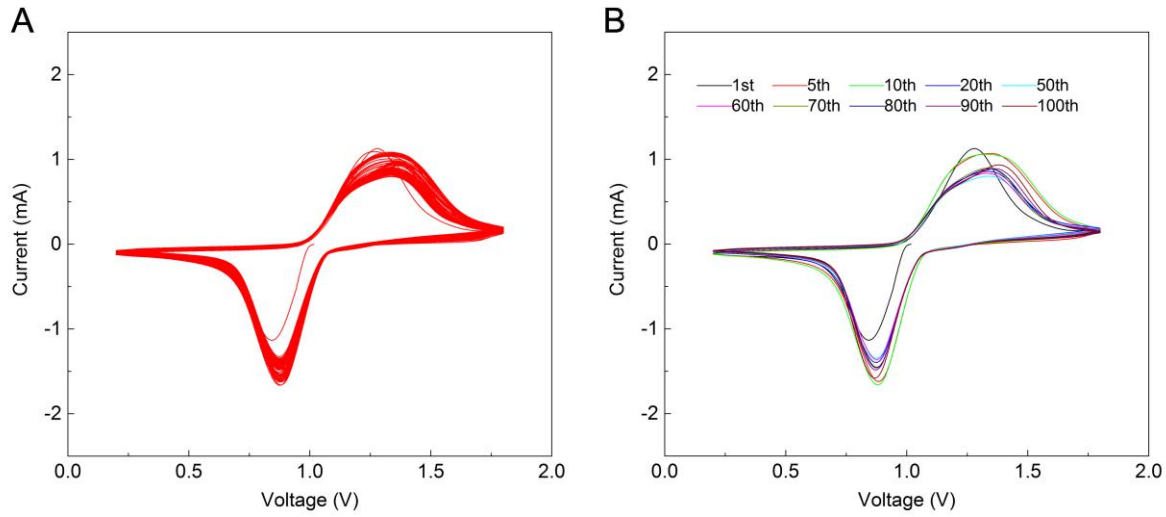

fig. S4. CV curves of Zn-C4Q battery at 0.5 mV s^{-1} for 100 cycles. (**A**) The total CV curves for 100 cycles. (**B**) The corresponding 1st, 5th, 10th, 20th, 50th, 60th, 70th, 80th, 90th, 100th CV curves.

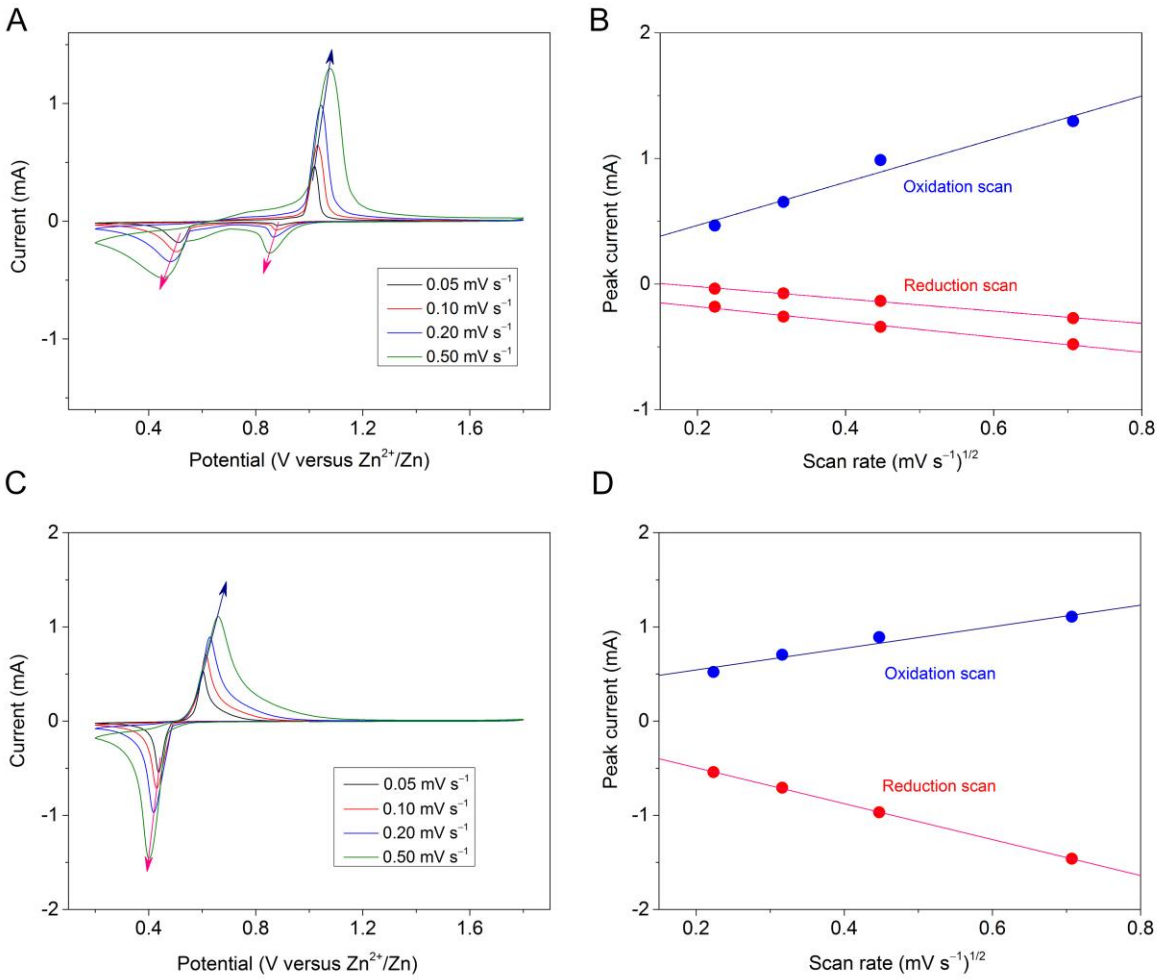

fig. S5. CV curves of other quinone compounds. (**A**) CV curves of Zn–9,10-PQ batteries at scan rates of 0.05, 0.10, 0.20, and 0.50 mV s^{-1}; (**B**) corresponding linear fit of the peak current and the square root of scan rate. (**C**) CV curves of Zn–9,10-AQ batteries at scan rates of 0.05, 0.10, 0.20, and 0.50 mV s^{-1}; (**D**) corresponding linear fit of the peak current and the square root of scan rate.

The reduction (Zn-ion uptake)/oxidation (Zn-ion removal) peak currents of both Zn–9,10-PQ and Zn–9,10-AQ batteries increase linearly with the square root of scan rates, which demonstrates that the electrochemical behavior is controlled by the diffusion process.

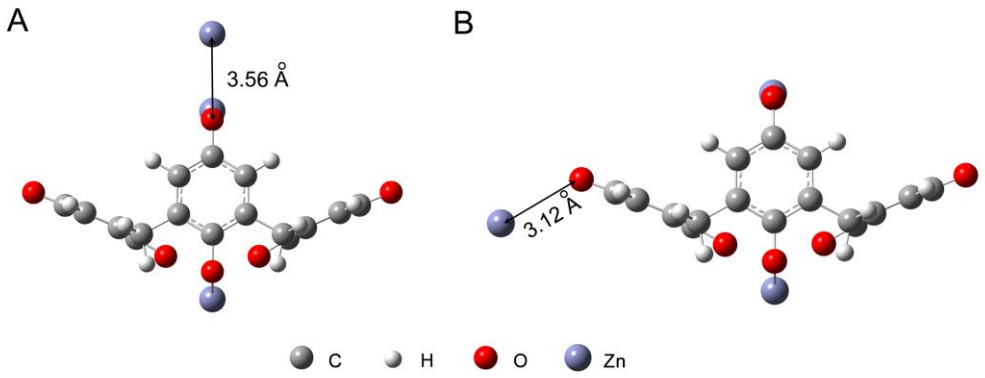

fig. S6. The uptake of the fourth Zn ion in the molecular structure of C4Q. (**A**) The Zn-ion uptake occurs on the top of Zn_3C4Q. (**B**) The Zn-ion uptake occurs on the side chain of Zn_3C4Q.

The fourth Zn-ion uptake on the top Zn_3C4Q delivers a theoretical discharge plateau of 0.08 V. The fourth Zn-ion uptake on the side chain of Zn_3C4Q corresponds to a theoretical discharge plateau of 0.03 V. Structure A is more stable between the two configurations suggested. However, the 4th Zn-ion has moved away from the C4Q molecule during the geometrical optimization process. After full optimization, the distance between the fourth Zn and nearest O is as far as 3.56 Å, indicating no Zn-O bond formation. Both the low plateau and the long Zn-O distance indicate the difficulty for the formation of Zn_4C4Q. Meanwhile, the distance of Zn-O in structure also largely exceeds the length of Zn-O bond (1.8 Å~2.4 Å) (*54*).

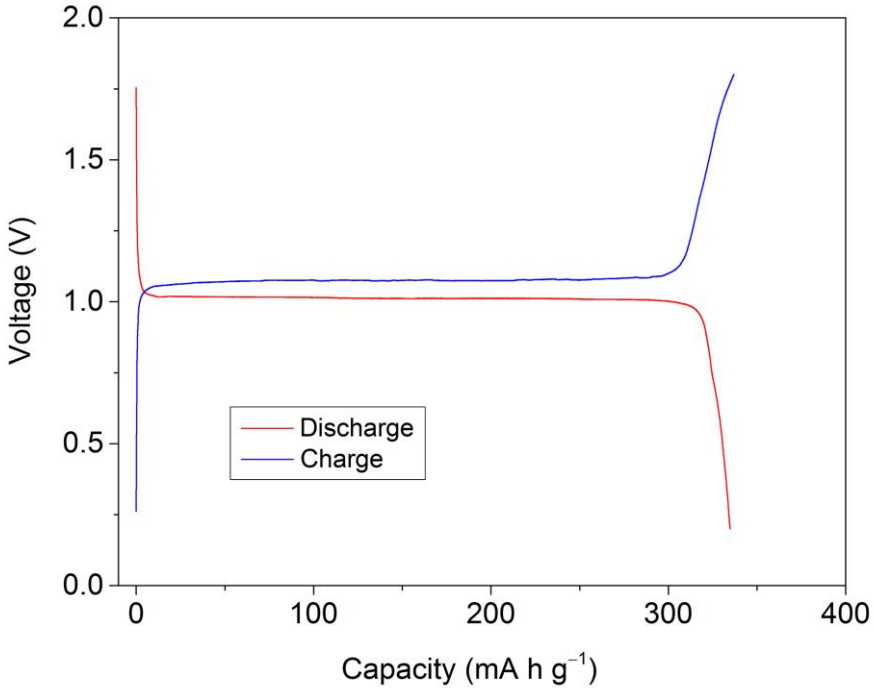

fig. S7. Discharge and charge curves of Zn-C4Q battery at 5 mA g^{-1}. The discharge capacity is about 337 mA h g^{-1} at low current density of 5 mA g^{-1}.

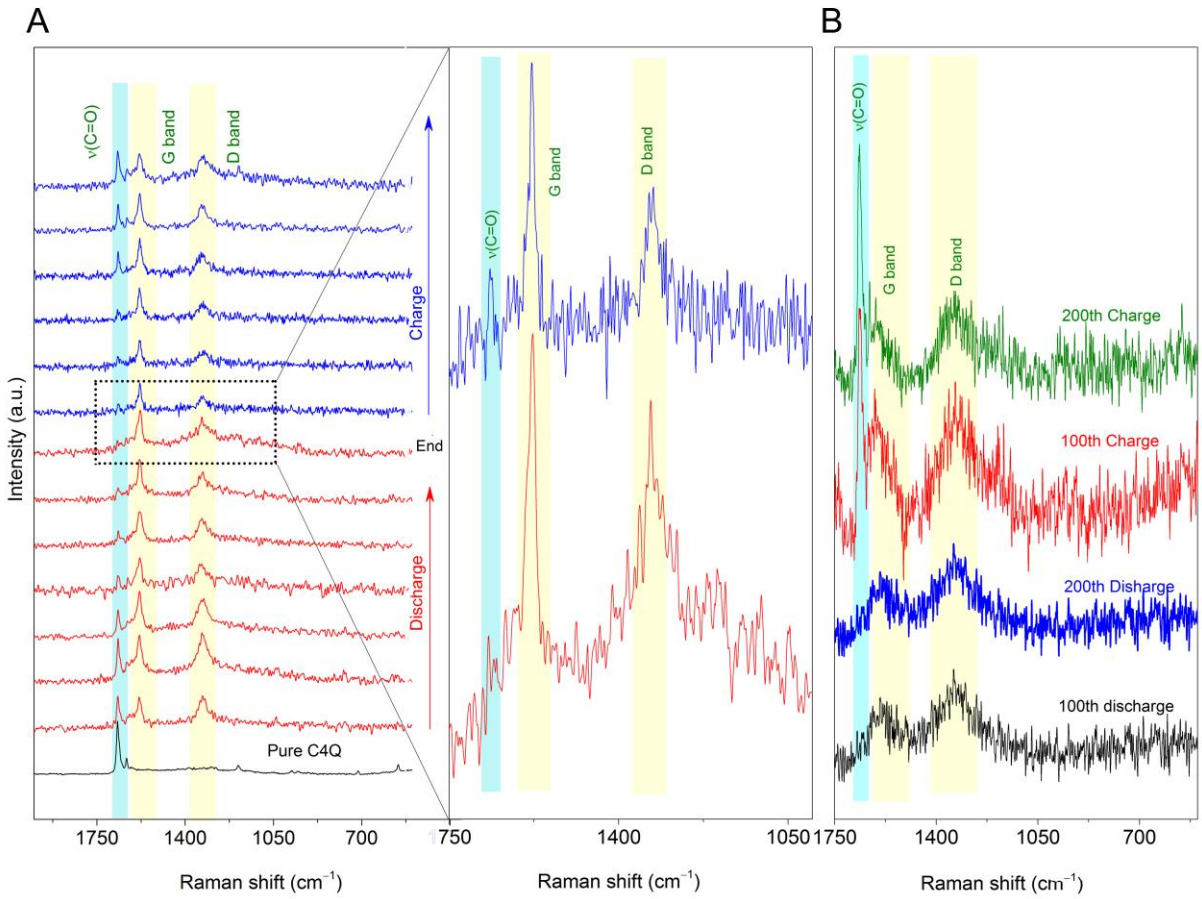

fig. S8. Raman characterizations of Zn-C4Q batteries. (**A**) In situ Raman characterizations of Zn-C4Q batteries (left) and corresponding enlarged part (Right). (**B**) Raman characterizations of discharged and charged C4Q cathode at 100th and 200th cycle.

The major peaks at 1670 cm^{-1} is the typical position of the C=O bond in quinone compound (*55*). At discharge process, this peak turns very weak but still exists after Zn-ion uptake and recurs to the original intensity after charge process. For comparison, the D band and G band of conductive additives remain unchanged. The reason of very weak signal at ~1670 cm^{-1} is also attributed to the shield of carbon's Raman signal and the uneven base line. This Raman evolution is well maintained at 100th and 200th cycle, indicating the good reversibility of C4Q cathode.

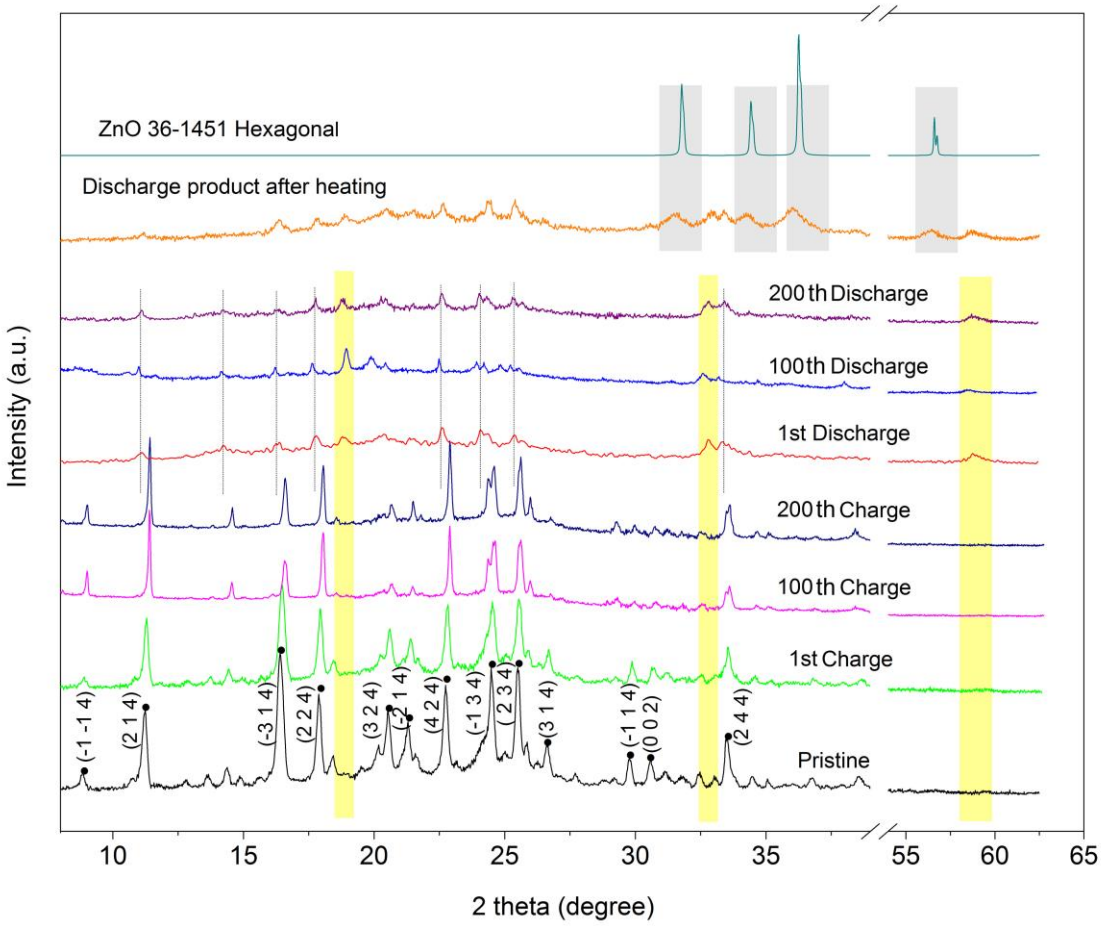

fig. S9. Ex situ XRD characterizations of Zn-C4Q batteries. C4Q belongs to monoclinic crystal system with P21/C point group, in which a=9.046 Å, b=21.955 Å, c=11.366 Å, β=104.90°, V=2181.3 $Å^3$ (*56*). The yellow band on the figure stands for the emerging peaks, indicating the phase change of C4Q after discharge, in accordance with that the heterogeneous two phases reaction results in the flat plateau characteristics. The intensity of all the peaks after discharge is reduced considerably, which is caused by the loss of active materials. Although the rinse of the electrode with water can wipe off the remained $Zn(CF_3SO_3)_2$ on the electrode in order to investigate the change of C4Q, it also wipe off some discharge product because it is a little soluble in water. In addition, we find that there are shift in the peaks after discharge. All the peaks shift to the low angles, which should be caused by zinc-ion uptake. Meanwhile, we

found the discharge product is not stable at high temperature. The peaks of ZnO emerge after heating at 80 ºC.

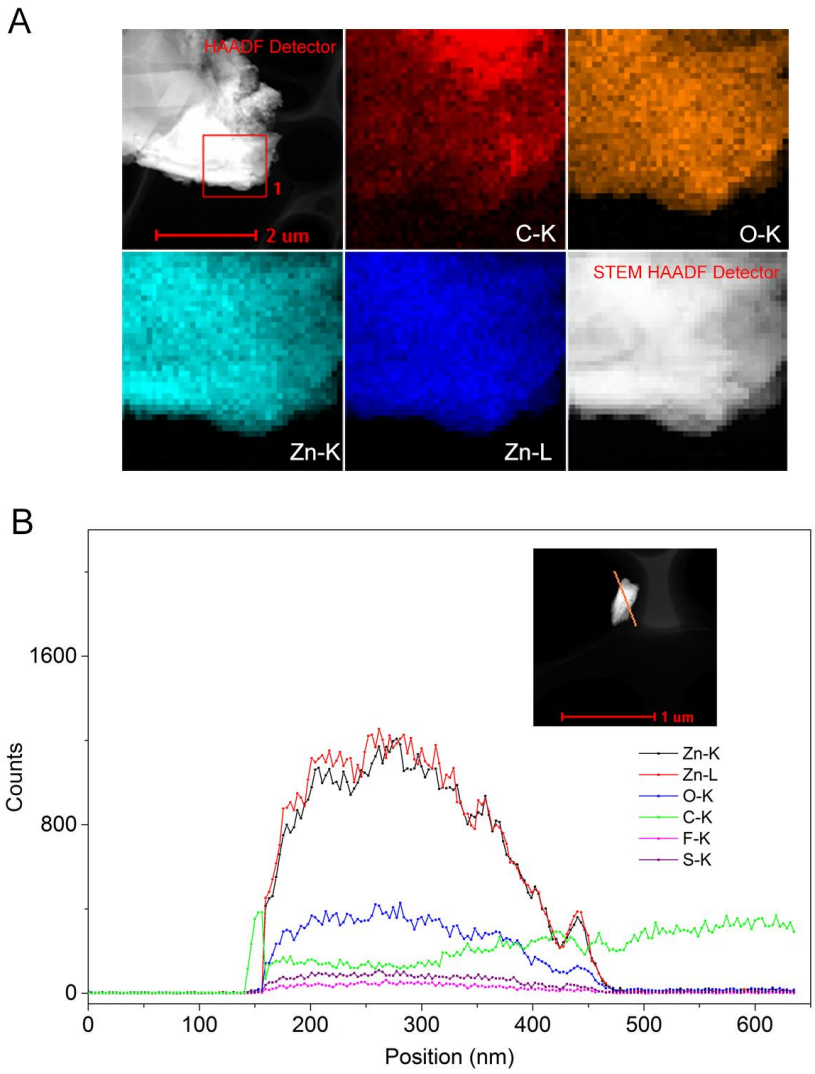

fig. S10. TEM characterization of C4Q electrode after discharge. (**A**) Element C, O and Zn mapping of C4Q electrode after discharge. (**B**) Line scanning of Zn, O, C, F and S of electrode after discharge.

TEM element mapping and line scanning show the major components of discharge product is C, O and Zn. Other components of F and S existed in electrolyte ($[Zn(CF_3SO_3)_2]$) are very

little, demonstrating that Zn existed in the discharged C4Q. At the high energy, some decomposition seems to occur on the sample. The distribution is homogenous for Zn and O, but it seems to be less carbon counts near the Zn regions in the mapping. This might be caused by the decomposition of discharge product and formation of ZnO under high kEV of TEM in accordance with the result of XRD after heating.

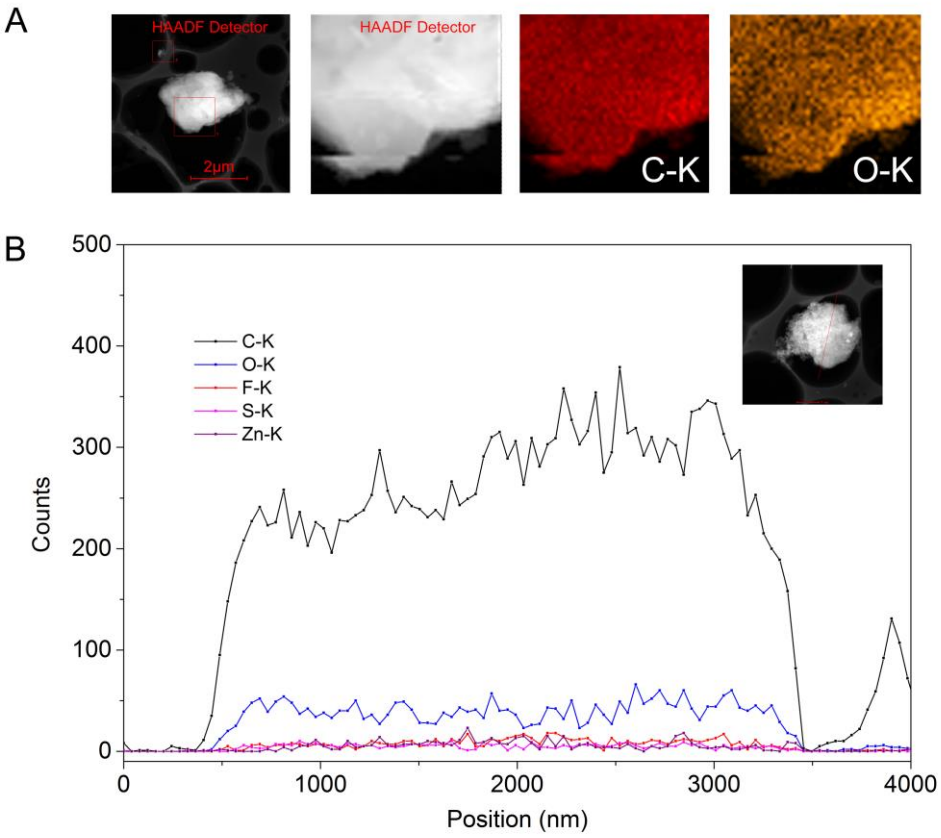

fig. S11. TEM characterization of C4Q electrode after charge. (**A**) Element C, O mapping of C4Q electrode after discharge. (**B**) Line scanning of C, O, F, S and Zn of electrode after discharge.

TEM element mapping and line scanning show the major compositions of charge product are C and O.

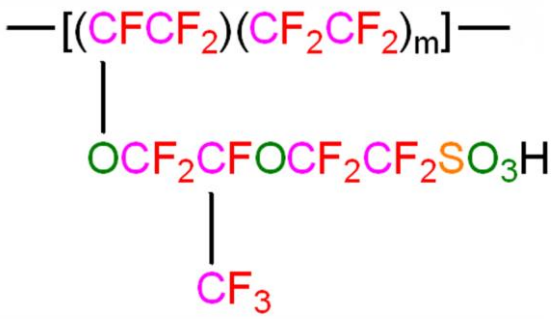

fig. S12. Composition of Nafion.

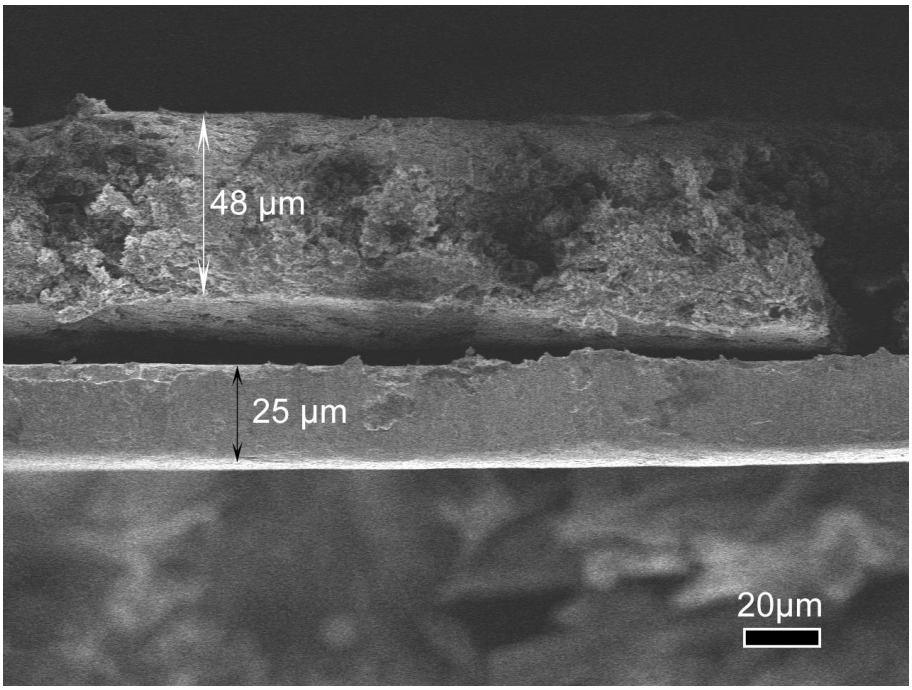

fig. S13. SEM images of the prepared C4Q cathode on titanium foil. The loading of active materials is ~2.5 mg cm^{-2}, corresponding to the areal capacity of ~0.8 mAh cm^{-2}. The typically used Ti foil current collector is about 25 μm and the thickness of active materials is about 48 μm.

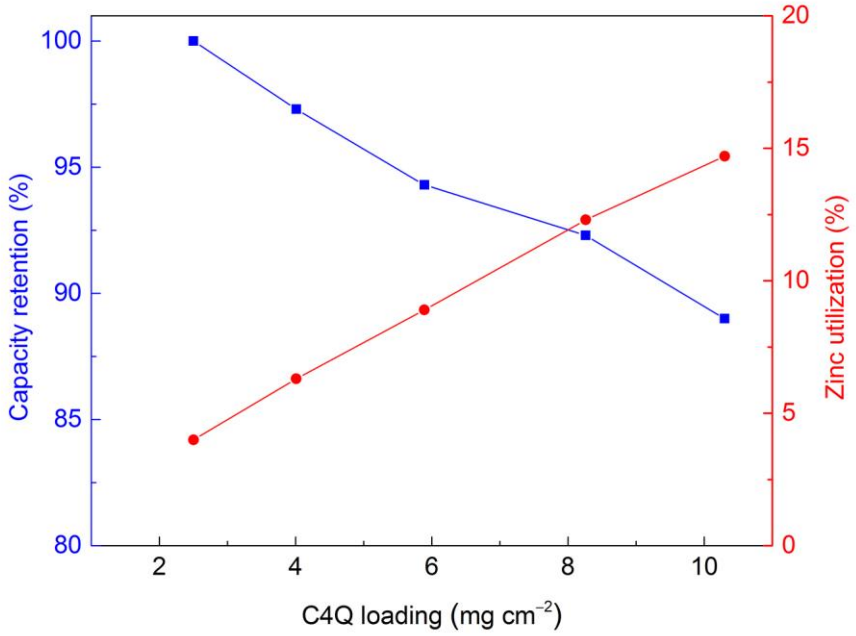

fig. S14. Capacity retention and zinc utilization using different loading masses of C4Q.

The zinc utilization increases with increasing the loading of C4Q. In addition, the capacity retention still maintains ~90% at a high loading mass up to 10 mg cm^{-2}.

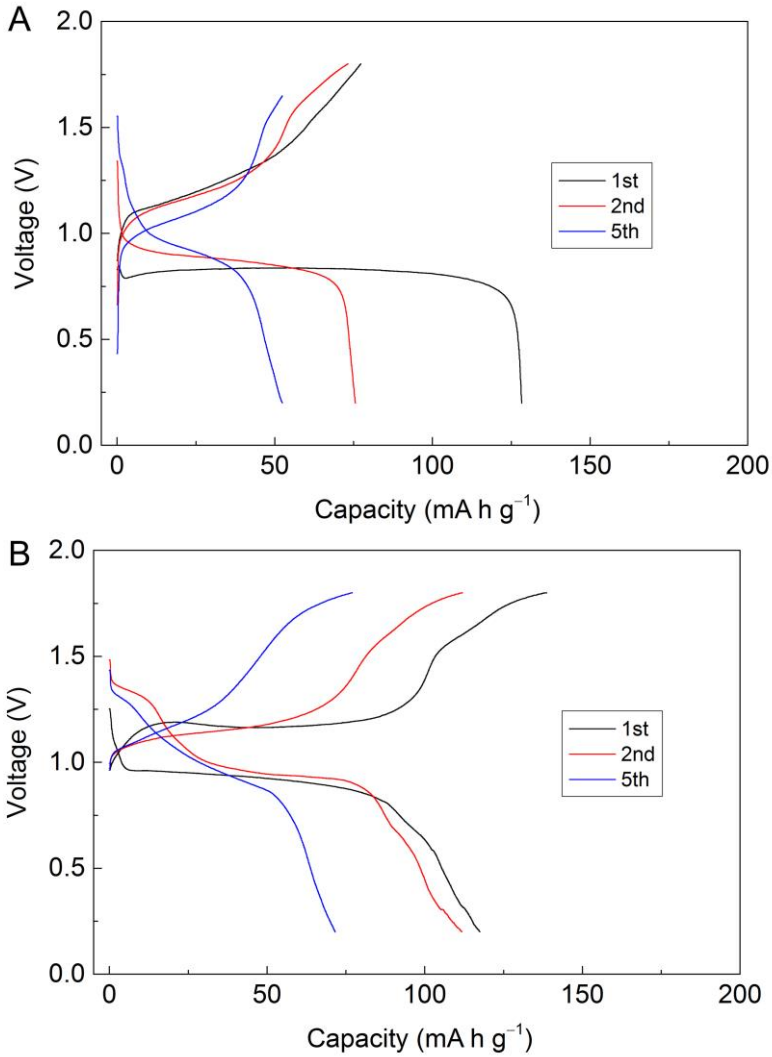

fig. S15. Electrochemical performance of Zn-C4Q batteries in organic electrolyte. (**A**) Filter paper and (**B**) Nafion membrane as separators.

The electrolyte is 0.2 M $Zn(CF_3SO_3)_2$ dissolved in dimethylsulfoxide. The dissolution is the most serious problem of quinone compounds in rechargeable batteries with organic electrolyte and some C4Q has already dissolved in electrolyte before electrochemical test. Therefore, the Zn-C4Q batteries with organic electrolyte show fast capacity fading, which display discharge specific capacities of 128, 76, and 52 mA h g^{-1} at the 1st, 2nd and 5th cycle, separately. Using Nafion membrane separator can partly improve the electrochemical performance, which shows the capacity of 118, 112, and 72 mA h g^{-1} at the 1st, 2nd and 5th

cycle, separately. C4Q is highly soluble in organic electrolyte, thus the influence of Nafion membrane in organic electrolyte is not as good as in aqueous electrolyte.

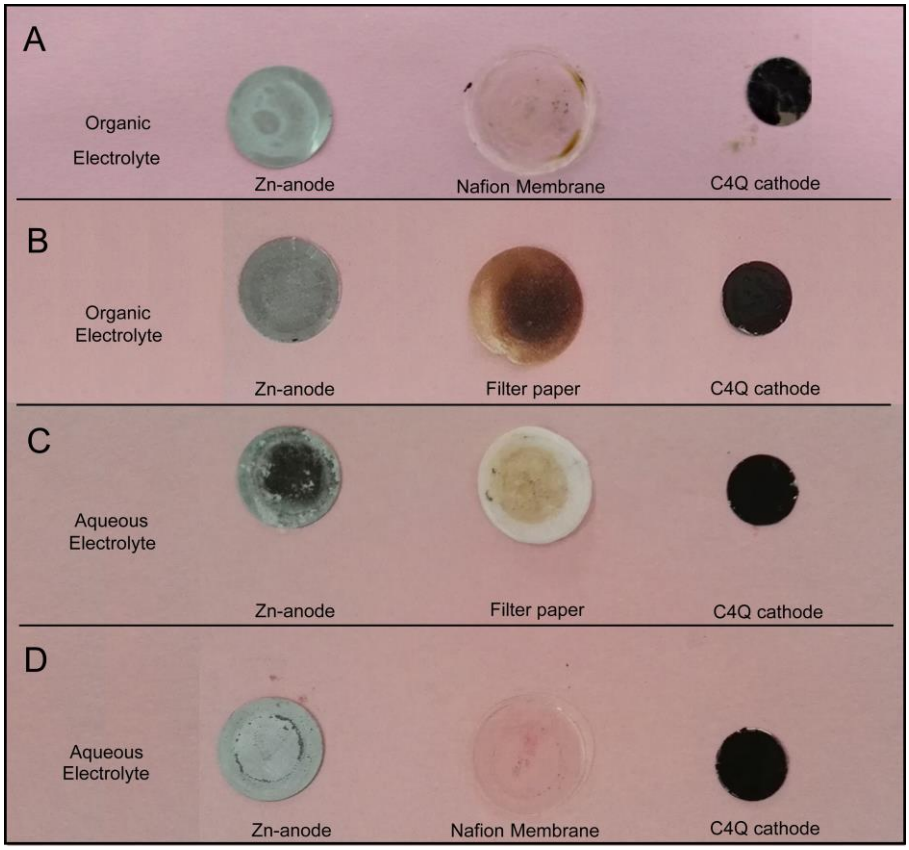

fig. S16. Digital photos of the Zn anode, separator (filter paper or Nafion membrane), and C4Q cathode after cycling. Digital photos of Zn-foil, (**A**) Nafion membrane or (**B**) filter paper and C4Q cathode after 5 cycles at fully charged states with organic electrolyte. Digital photos of Zn-foil, (**C**) filter paper or (**D**) Nafion membrane and C4Q cathode after 30 cycles at fully charged states with aqueous electrolyte.

The filter paper turns obviously brown due to the dissolution of C4Q in organic electrolyte. The color of Nafion membrane also changes in organic electrolyte. In comparison, the Zn–C4Q batteries operated under aqueous electrolyte display less dissolution. In particular,

the aqueous Zn–C4Q batteries with Nafion separator show both restrained dissolution and well-protected Zinc anode.

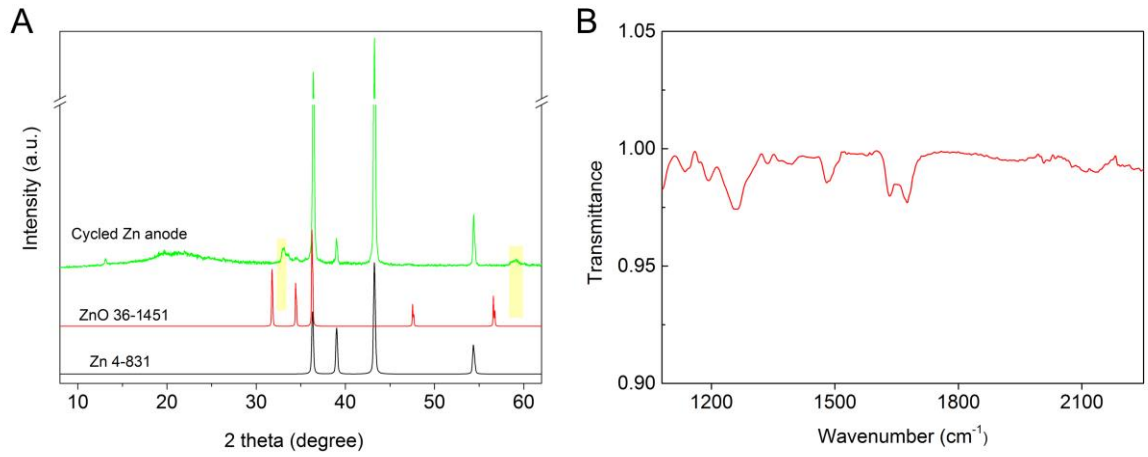

fig. S17. Characterization of the zinc anode after cycling using a filter paper separator. (**A**) XRD pattern of zinc anode after cycling. (**B**) ATR-FTIR spectra of zinc anode after cycling**.**

According to the pattern of XRD, the major composition is still zinc after discharge. While the peaks at about 33° and 60° (yellow region) share similarity with the discharge product. In addition, the FTIR spectra also confirm this result. Typical vibrations of carbonyl and $–CH_2–$ are investigated, proving the product formed on the surface of zinc belongs to the Zn_xC4Q. This phenomenon is supposed to be caused by the soluble discharge product $C4Q^{2x-}$, which will shuttle to the zinc side and generate by-product.

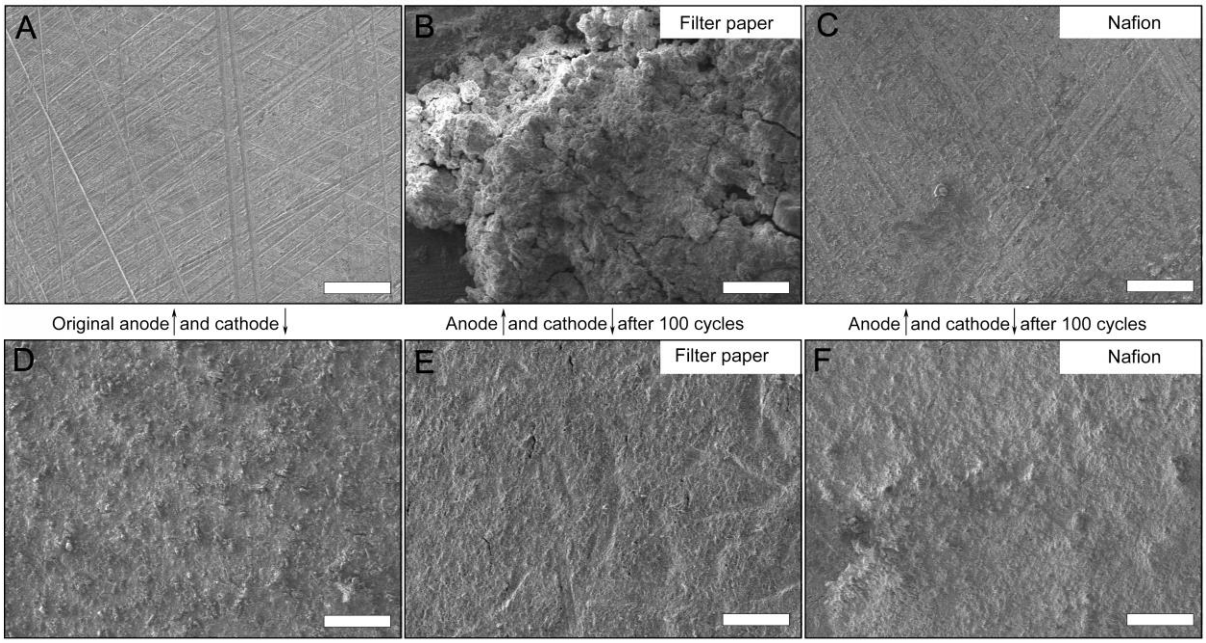

fig. S18. SEM images of electrodes before and after cycles. Original (**A**) anode and (**D**) cathode. (**B**) anode and (**E**) cathode with filter paper separator after cycling 100 times. (**C**) anode and (**F**) cathode with Nafion membrane separator after cycling 100 times. Scale bar 100 μm.

SEM images show that the morphology of cathode turns flat after cycling, which is proposed as the gradual nanosizing through repeatedly cycling. In comparison, the surface of Zn anode coupled with filter paper undergoes serious damage with a large amount of by-products. However, the Zn anode coupled with Nafion membrane is still smooth after 100 cycling.

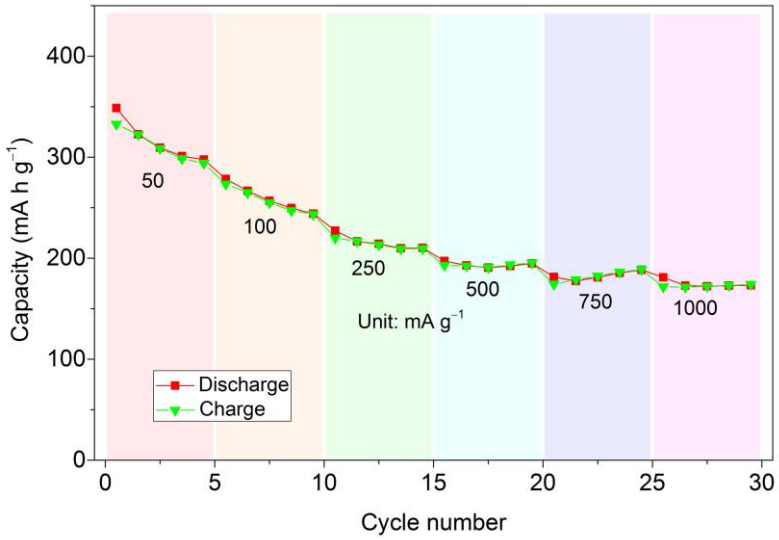

fig. S19. Rate performance of Zn-C4Q batteries with a Nafion separator. The specific capacities are 333, 273, 220, 197, 174 and 172 mA h g^{-1} at the current density of 50, 100, 250, 500, 750, and 1000 mA g^{-1}, respectively. The composition of electrode is C4Q, Super P conductive additives, and polyvinylidene fluoride (PVdF) with weight ratio of 6:3.5:0.5.

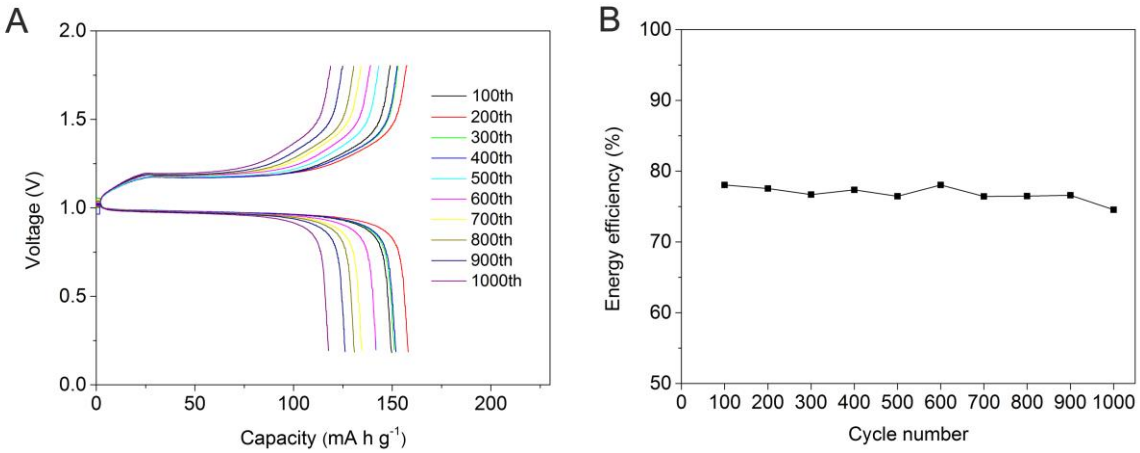

fig. S20. Galvanostatic discharge and charge curves with selected cycles at 500 mA g^{-1} and corresponding energy efficiency.

The discharge and charge curves remained similar shape after 1000 cycles. While the polarization increases after increasing the current density and the energy efficiency is about 80 %.

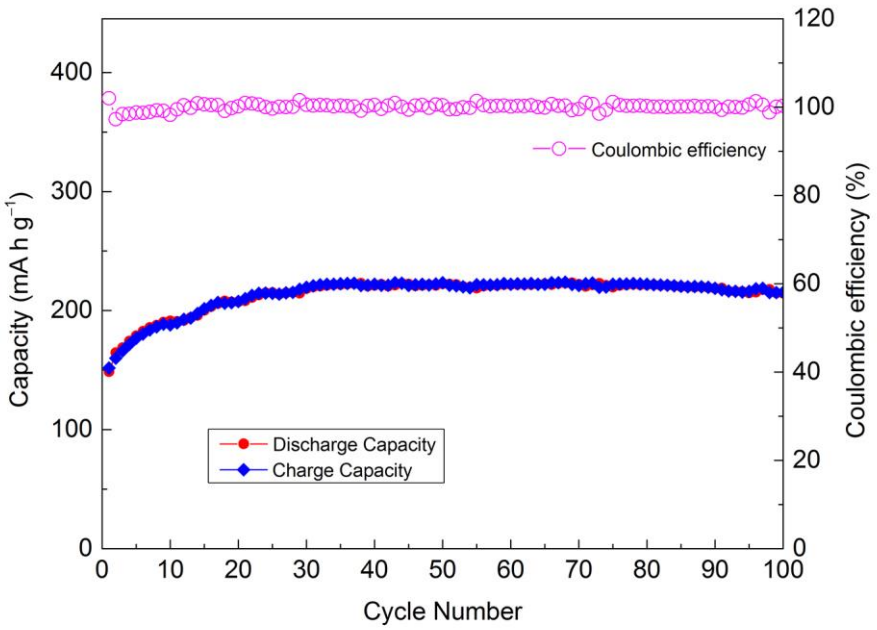

fig. S21. Cycling performance of Zn-C4Q battery using C4Q cathode with a higher conductive carbon ratio (60 wt %). After increasing the contents of conductive carbon, the capacity increases to 215 mA h g^{-1} at 100th cycle at current density of 500 mA g^{-1}.

fig. S22. Exhibition of pouch cells. The picture at the upper right corner is typically prepared zinc anode and C4Q cathode. The shape and numbers of electrodes can be changed to adjust different capacity of pouch cells. Stack technology is used to assemble the pouch cell (*58*). The constituents of batteries are placed with the unit of Zn anode/separator/cathode. These units are paralleling together to form the final pouch cell. The cell is sealed with plastic membrane.

The pouch cell with designed capacity of 0.1 Ah applied cathode containing 350 mg C4Q, in which the theoretical capacity is 117.6 mA h (0.35 g × 336 mA h g^{-1}). In practical test, the pouch cell displayed a capacity of 105 mA h after discharging to the voltage of 0.8 V, corresponding to the 89 % depth of discharge (DOD) of C4Q compared with theoretical capacity (105 ÷117.6 × 100%). Meanwhile, the theoretical consumption of zinc anode is 0.128

g (105 mA h ÷ 820 mA h g^{-1}) to generate the capacity of 105 mA h. Therefore, the energy density of pouch cell calculated by C4Q cathode and theoretical Zn anode is 220 Wh kg^{-1} {(0.105 A h × 1 V) ÷ [(0.35 + 0.128) × 10^{-3} kg]}. The practical mass of zinc foil can be as low as 0.26 g, thus the practical utilization of zinc anode is up to 49% in pouch cells.

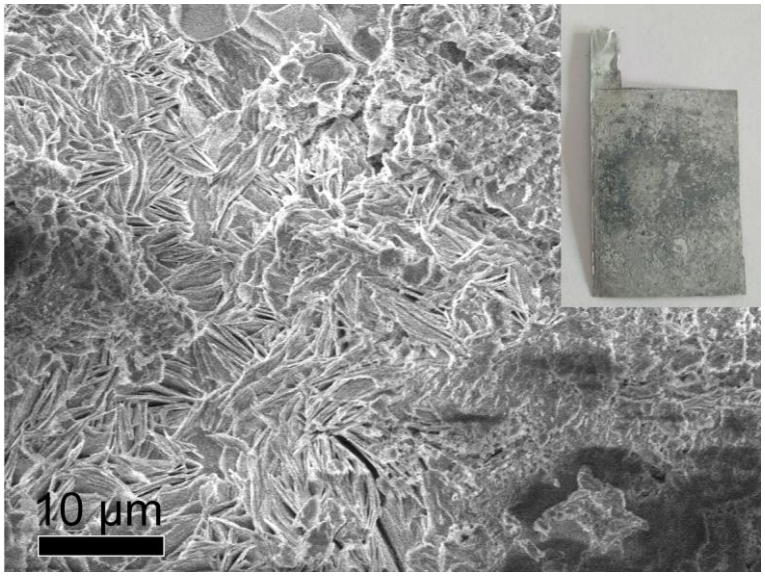

fig. S23. Digital photo and SEM image of the zinc anode after cycling in pouch cells. The pouch cell uses a high loading of C4Q (about 20 mg cm^2, 10 mg cm^2 at each side), resulting to a higher utilization and serious morphology change of zinc anode.

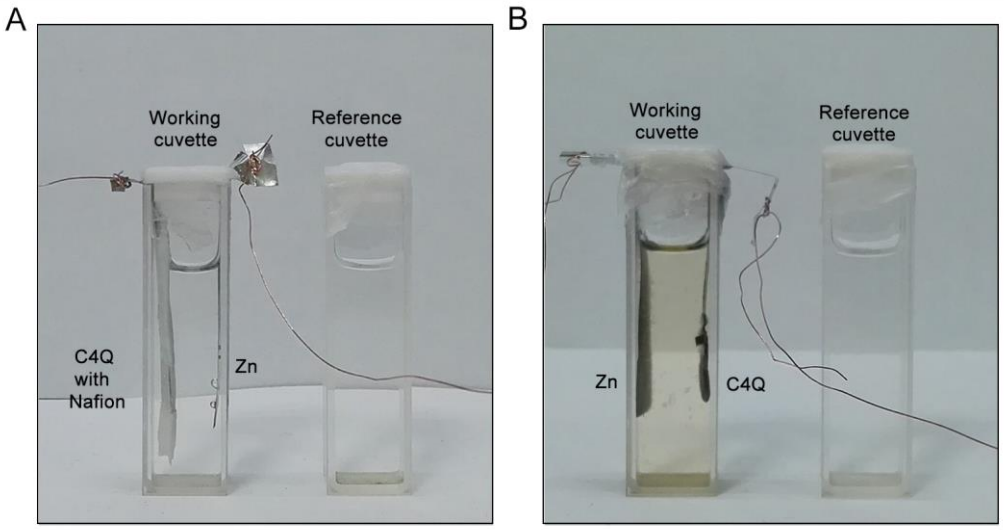

fig. S24. Digital photos of designed batteries after in situ UV-vis spectrum collections. (**A**) Cycled Zn–C4Q battery with Nafion membrane coating on the surface of C4Q. No color changes in the solution, indicating the inhibition of dissolution. (**B**) Cycled Zn–C4Q batteries without Nafion membrane, the solution turn light brown owing to the dissolution of active species.

The cuvette is reformed as an in situ electrochemical cell. Both solutions in working and reference cuvettes are 3M $Zn(CF_3SO_3)_2$ in H_2O. These reformed batteries are discharged and charged at the current density of 100 mA g^{-1}. Synchronously, the UV-Vis spectra are collected every ten minutes.

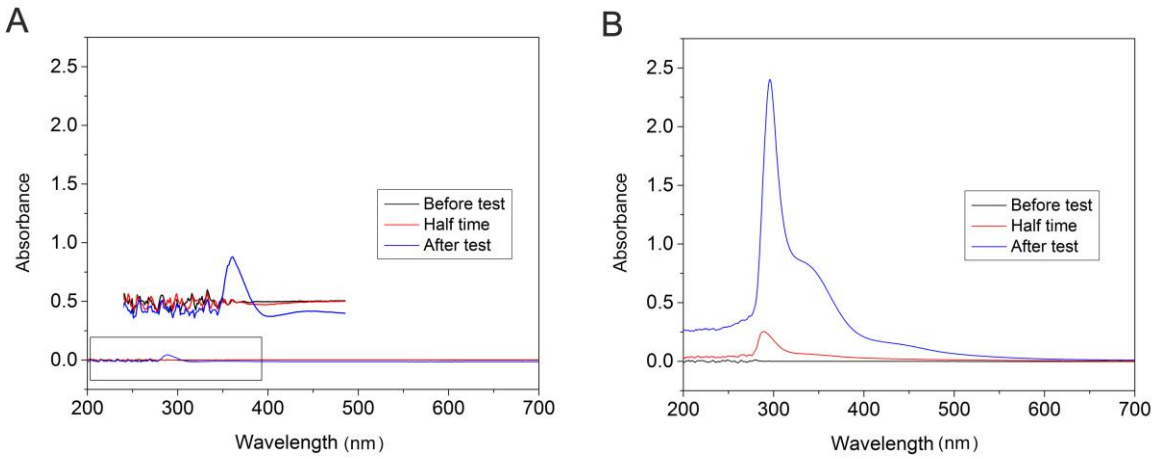

fig. S25. Selected two-dimensional UV-vis spectra.

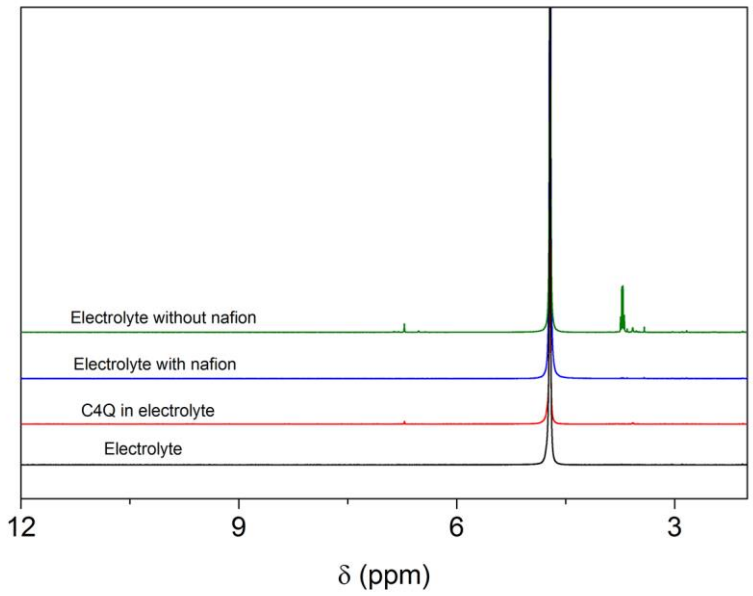

fig. S26. ^{1}H NMR spectra of different electrolytes after cycling in batteries used for the UV-vis test. In order to confirm the soluble product in the electrolyte, we prepared the electrolyte of 3M $Zn(CF_3SO_3)_2$ in deuterium oxide (D_2O). The pure electrolyte only shows the peak of D_2O (black line). And pure C4Q is hardly soluble in electrolyte (red line). In addition, the electrolyte with Nafion protection of cathode also only shows the peak of D_2O.

However, without the production of Nafion, two obvious peak areas at about 6.7 ppm and 3.5 ppm emerge, corresponding to the peak of H in framework of C4Q. Considering the C4Q is hardly soluble in electrolyte and the reaction happen on carbonyl, we deduce the soluble product belong to the species of $C4Q^{2x-}$.

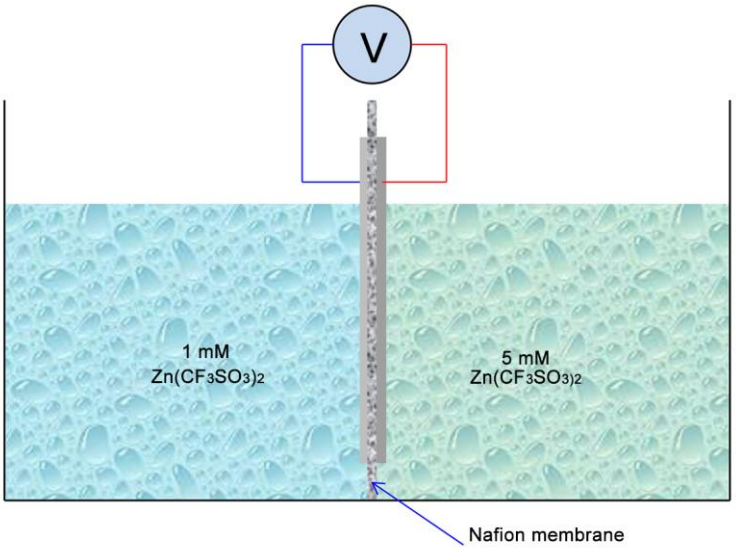

fig. S27. Membrane potential tests. Electrolyte with different concentration of salts are separated with Nafion membrane in order to test the membrane potential.

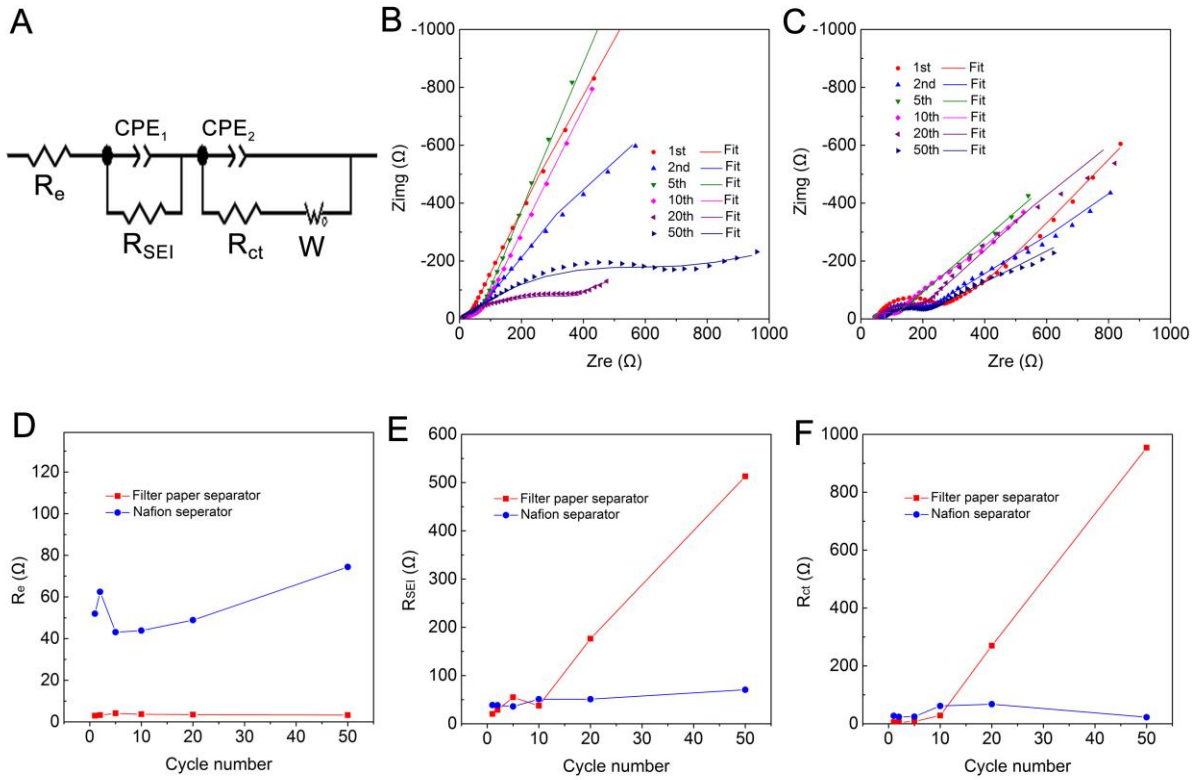

fig. S28. EIS of Zn-C4Q batteries. (**A**) an equivalent circuit diagram of EIS. EIS spectra and fitting curves of Zn-C4Q batteries with (**B**) filter paper separator and (**C**) Nafion membrane separator. (**D**) Electrolyte resistance (R_e), (**E**) solid-electrolyte interface resistance (R_{SEI}) and (**F**) charge-transfer resistance (R_{ct}) comparisons.

The EIS is obtained on the fully charged state of Zn-C4Q batteries at the temperature of 25 °C. Although the batteries with filter paper as the separator show smaller R_e due to the good impregnation of electrolyte benefiting from the macroporous character. While, due to the side reaction and by-product deposition on the anode, the SEI and charge-transfer resistance sharply increases with long-term cycling. In contrast, the resistance of the battery with Nafion membrane barely changed with cycling.

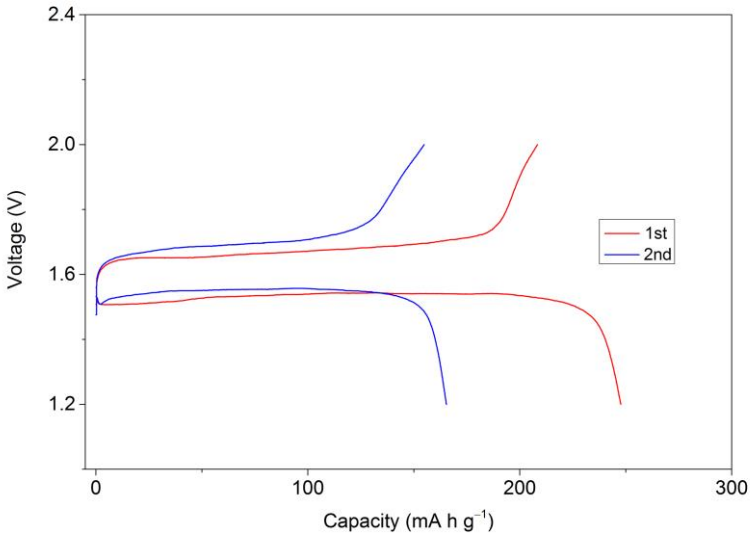

fig. S29. Electrochemical performance of aqueous Mg-C4Q batteries. The Mg–C4Q battery is tested with the electrolyte of 3 M $Mg(CF_3SO_3)_2$ in water and anode of metal Mg, the current density is 20 mA g^{-1}. The Mg–C4Q battery shows a capacity of 247.4 mA h g^{-1} with discharge potential of 1.54 V. Owing to the sluggish kinetic and instability of metal Mg in aqueous electrolyte, the electrochemical properties are still to be enhanced. However, this result clearly proves the universality of quinone compounds in aqueous electrolyte.

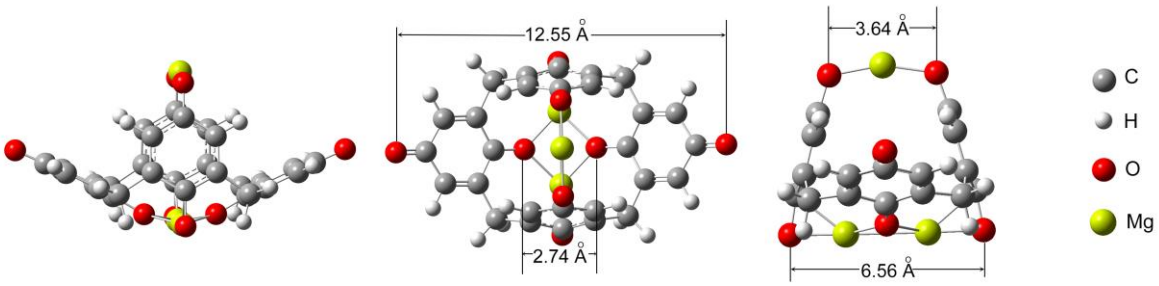

fig. S30. Structure of C4Q after uptake of three Mg ions. The distance between oxygen atoms has been labeled with unit of angstrom.

table S1. Maximum specific capacity and lowest discharge/charge gap of electrodes coupled with metal zinc in aqueous batteries.

Electrode materials	Maximum capacity [a]	Lowest gap[b]	Ref vs Notes
Cu^{2+} intercalated Bi-birnessite	617 mA h g^{-1}	150 mV	(*27*, *28*)
calix[4]quinone (C4Q)	**335 mA h g^{-1}**	**70 mV**	This work
α-MnO_2	325 mA h g^{-1}	200 mV	(*19*)
γ-MnO_2	325 mA h g^{-1}	200 mV	(*22*)
$Zn_{0.25}V_2O_5 \cdot nH_2O$	300 mA h g^{-1}	120 mV	(*23*)
$Zn_xMo_{2.5+y}VO_{9+z}$	220 mA h g^{-1}	600 mV	(*25*)
α-MnO_2	210 mA h g^{-1}	300 mV	(*18*)
9,10-AQ	**194 mA h g^{-1}**	**40 mV**	This work
Cation-deficient $ZnMn_2O_4$	150 mA h g^{-1}	200 mV	(*24*)
1,4-NQ	150 mA h g^{-1}	110 mV	This work
$FeFe(CN)_6$	120 mA h g^{-1}	500 mV	(*29*)
9,10-PQ	112 mA h g^{-1}	360 mV	This work
1,2-NQ	69 mA h g^{-1}	220 mV	This work
$Zn_3[Fe(CN)_6]_2$	65 mA h g^{-1}	130 mV	(*30*)
$Na_{0.95}MnO_2$	60 mA h g^{-1}	300 mV	(*26*)
$KCuFe(CN)_6$	53 mA h g^{-1}	70 mV	(*31*)

Maximum capacity is obtained from capacity at the lowest current density reported from the references. [b] The value of lowest gap is according to the description of the related references.

If the works haven’t listed the gap value directly, we estimated this value through measuring the potential gap between the half of discharge and charge capacity, respectively.